Rock Mechanics and Rock Engineering (2023) 56:3339–3357
https://doi.org/10.1007/s00603-023-03227-0

ORIGINAL PAPER

AE/MS Event Source Location for Circular Hole-Contained Structures Through an Analytical Solution-Based Shortest P-Wave Travel Path

Xueyi Shang[1] · Caiyun Liu[1] · Xibing Li[2] · Linqi Huang[2]

Received: 31 July 2022 / Accepted: 7 January 2023 / Published online: 28 January 2023

Abstract

Acoustic emission/microseismic (AE/MS) source location plays a vital role in the safety monitoring of circular hole-contained structures (e.g., tunnels, pipelines, and pressure vessels). However, traditional methods may obtain a bad P-wave travel path and poor source location accuracy. To handle this, an analytical solution-based shortest P-wave travel path and a grid search-based AE/MS event source location method are proposed for circular hole-contained structures. Moreover, the objective function of AE/MS source location considers the P-wave arrival time system error. Both synthetic tests and pencil-lead break (PLB) application tests in 2D and 3D circular hole-contained structures show the outperformance of the proposed location methods. First, the analytical method obtains an equal or smaller P-wave travel distance than that of the Dijkstra and A* algorithms, which means the analytical method generates better theoretical data. Then, the average location errors of PLB events for the 2D circle-contained rectangle, 3D full circular hole-contained cuboid, and 3D part circular hole-contained cuboid are 0.57 cm, 1.87 cm, and 2.25 cm, respectively. These location results are better than results based on the shortest P-wave paths of the straight line, Dijkstra, and A* algorithms. Moreover, the proposed method solves that former analytical solutions do not consider the thickness of cylindrical shell structures.

Highlights

- An analytical solution-based shortest P-wave travel path has been proposed for circular hole-contained structures.
- The acoustic emission/microseismic source location objective function considers the P-wave arrival time system error.
- The average location errors of pencil-lead break events for circular hole-contained structures are within 2.25 cm.
- The analytical solution-based location method obtains better location results than methods based on the straight line, Dijkstra and A* algorithms.

Keywords Acoustic emission · Microseismic · Source location · Hole-contained structure · Shortest path

1 Introduction

Circular hole-contained structures have good stability and have been widely used in tunnels, pipelines, and pressure vessels. However, they may suddenly break due to stress wave disturbance, fatigue damage, and longtime pressure, threatening human life and property. An acoustic emission/microseismic (AE/MS) monitoring system can record the micro-rupture signal before a structural failure and provide an early warning. It has been widely used in structural health monitoring (Koabaz et al. 2012), where an accurate source location is a basis. The objective function of source location is usually built from P-wave travel time. However, the commonly used straight line-based AE/MS location is unsuitable

✉ Xueyi Shang
shangxueyi@cqu.edu.cn

[1] State Key Laboratory of Coal Mine Disaster Dynamics and Control, School of Resources and Safety Engineering, Chongqing University, Chongqing 400044, China

[2] School of Resources and Safety Engineering, Central South University, Changsha 410083, China

for a hole-contained structure. For example, circular holes were built in the Jinping II hydropower station, there are many events far away from the tunnels for the straight line-based MS location results (Feng et al. 2015a, b), which indicates that poor MS events location results have been obtained for hole-contained structures. Other studies get similar results (Dong et al. 2020; Hu and Dong 2020). The main failure reasons for straight line-based location results of hole-contained structures include: (1) the empty zone makes that the first arrived P-wave of each signal may not travel along the straight line between the source and sensor; and (2) the heterogeneity of a complex structure makes the fixed speed-based location fail.

(1) Straight line-based location in complex structures.

Unlike the traditional straight line-based location method that uses a constant and known P-wave velocity, Dong et al. (2015; 2020) treat P-wave velocity as an unknown parameter and solve it in each source location inversion, Kundu et al. (2012) divide sensors into groups by interaction distance before a source location. Both approaches reduce the influence of velocity heterogeneity. By contrast, some researchers focus on the quality improvement of P-wave arrival data, and various noise reduction methods and P-wave arrival picking methods have been proposed (Shang et al. 2018; Mborah and Ge 2018; Peng et al. 2021). Moreover, the P-wave arrival time system error (PATSE) is eliminated in Shang et al. (2022) and Jiang et al. (2021a). For a given P-wave arrival dataset, Li et al. (2016) proposed an exponential decay-based location objective function to reduce the effect of large picking errors, and Zhou et al. (2021) applied a variety of optimization algorithms to solve this function. Moreover, Dong et al. (2019), Rui et al. (2022), and Peng et al. (2022) chose the initial location result to eliminate poor P-wave arrival data. The location points of P-wave arrival combinations and density characterization algorithms are then combined to determine an event location, ensuring a stable location result (Peng et al. 2022). These methods have improved the accuracy and stability of an AE/MS location. However, there are usually large P-wave travel differences between the straight line path and the shortest path in a complex structure, resulting in low location accuracy.

(2) Non-straight line-based location in complex structures.

Many studies that follow the Snell's ray path law have been done on the AE/MS source location for a one-dimensional layered velocity model (Gesret et al. 2015). However, this velocity model is quite different from a hole-contained structure. Baxter et al. (2007) obtained the P-wave relative travel time dataset through many pencil-lead break (PLB) events, which can ensure the quality of P-wave travel time in a complex structure. However, the experimental process is very time-consuming. Dong et al. (2020; 2022), Peng et al. (2020), and Jiang et al. (2021b) computed theoretical P-wave travel time using an improved A* algorithm and fast marching method (FMM), which can be adopted to a variety of complex structures. However, these search algorithms may obtain a local optimal path, and the gridding process will cause errors in the P-wave travel path (Dong et al. 2020). Analytical solutions have been done on cylindrical shell structures to obtain a theoretical P-wave travel distance. In this method, the sensor and source are projected onto one circular side. Then the length of the circular arc and horizontal coordinate difference following the Pythagorean theorem are used to obtain the shortest P-wave travel distance on a cylindrical shell structure (Wang et al. 2021). However, a circular hole-contained structure usually has a specific thickness, and the above analytical solution has a limited application field.

(3) How will this work address the above problems?

The above review shows that it is necessary to propose a universal analytical solution for circular hole-contained structures. In this study, an analytical solution has been proposed to find the shortest P-wave travel distance for circular hole-contained structures, and a grid search-based location method has been applied to verify its effectiveness. The main innovations and contributions of this study include: (1) solid geometry and projection methods are used to determine the spatial location relationship between the circular hole and line that connects the source and sensor. Then, analytical solutions of the shortest P-wave travel path for 2D circle-contained plane, 3D full circular hole-contained cuboid, and 3D part circular hole-contained cuboid are obtained; (2) a fastest P-wave travel time dataset is generated by the analytical method and reciprocity theorem. An objective function that combines the L1 norm time difference and P-wave arrival time system error is then established for an AE/MS event locating; and (3) the proposed location method achieves good results both in synthetic tests and PLB events. The average location errors of PLB events for 2D circle-contained rectangle, 3D full circular hole-contained cuboid, and 3D part circular hole-contained cuboid separately are 0.57 cm, 1.87 cm, and 2.25 cm, which are smaller than those of the straight line, Dijkstra and A* algorithms.

2 Proposed Location Method

2.1 P-wave Travel Path Computation

An accurate P-wave travel path is the basis of an AE/MS source location for circular hole-contained structures. There are several common cases, including a 2D circle-contained

rectangle, a 3D full circular hole-contained cuboid, and a 3D part circular hole-contained cuboid. The first and second cases can be treated as the special cases of the third case, the 3D full circular hole-contained cuboid can simulate structures such as pipelines, while the part circular hole-contained 3D structure can simulate a circular tunnel under construction.

2.1.1 2D Circle-Contained Rectangle

Suppose the locations of source A and sensor B in the 2D circle-contained rectangle separately are (x_0, z_0) and (x_i, z_i), and i is the sensor id. There are three spatial location relations (separation, tangency, and intersection, Fig. 1) between the circle and the line that connects the source and sensor. The workflow for obtaining the shortest P-wave travel path is shown as Fig. 2b1.

The perpendicular distance from the circular center to the line determined by the source and sensor is calculated through the following steps:

First, the straight line equation can be given as:

$$z = k(x - x_0) + z_0, \tag{1}$$

where $k = (z_i - z_0)/(x_i - x_0)$.

Then, Eq. (1) can be converted into $ax + bz + c = 0$, where $a = k$, $b = -1$, $c = -kx_0 + z_0$. Thus, the perpendicular distance from the circle center (x_c, z_c) to the straight line is given as:

$$d = \frac{|a \times x_c + b \times z_c + c|}{\sqrt{(a^2 + b^2)}}. \tag{2}$$

(a) If $d \geq r$, the straight line is separated or tangent to the circular hole (Fig. 1a), Thus, the shortest P-wave travel distance is equal to the straight line distance from the source to the sensor:

$$L^i_{\min} = \sqrt{(x_i - x_0)^2 + (z_i - z_0)^2}. \tag{3}$$

(b) If $d < r$, the connection line (Fig. 1c) or its extension line (Fig. 1b) determined by the source and sensor intersects the circular hole. To determine whether the connection line or its extension line intersects the circular hole, the lengths of the triangle sides (|AB|, |OA|, and |OB|) are calculated from the coordinates of source A, sensor B, and circular center O. Then, the ∠OAB and ∠OBA are obtained through Eqs. (4) and (5). If both the ∠OAB and ∠OBA are acute angles, the connection line intersects the circular hole (Fig. 1c); Otherwise, the extension line intersects the circular hole (Fig. 1b).

$$\angle \mathrm{OAB} = \arccos \frac{|\mathrm{AB}|^2 + |\mathrm{OA}|^2 - |\mathrm{OB}|^2}{2|\mathrm{AB}| \times |\mathrm{OA}|}, \tag{4}$$

$$\angle \mathrm{OBA} = \arccos \frac{|\mathrm{AB}|^2 + |\mathrm{OB}|^2 - |\mathrm{OA}|^2}{2|\mathrm{AB}| \times |\mathrm{OB}|}, \tag{5}$$

where $\angle \mathrm{OAB} \in [0,\ \pi]$ and $\angle \mathrm{OBA} \in [0,\ \pi]$.

If the extension line intersects the circular hole, Eq. (3) is used to calculate the $L^i_{\min}$. When the connection line passes through the circular hole, the $L^i_{\min}$ is calculated by the following steps:

Set the tangent point coordinates from the source to the circular hole as (xe_{i0}, ze_{i0}), then:

$$\begin{cases} (xe_{i0} - x_c)^2 + (ze_{i0} - z_c)^2 = r^2 \\ (x_0 - x_c)(xe_{i0} - x_c) + (z_0 - z_c)(ze_{i0} - z_c) = r^2 \end{cases}. \tag{6}$$

There are two tangent points from one point to a circle. In other words, Eq. (6) has two solutions M (xe_{i1}, ze_{i1}) and M′ (xe'_{i1}, ze'_{i1}).

Then, the coordinates of tangent points N (xs_{i1}, zs_{i1}) and N' (zs'_{i1}, zs'_{i1}) between the sensor and circular hole can be calculated in the same way. Thus, there are four possible P-wave travel paths, and their lengths are AM + MN + NB,

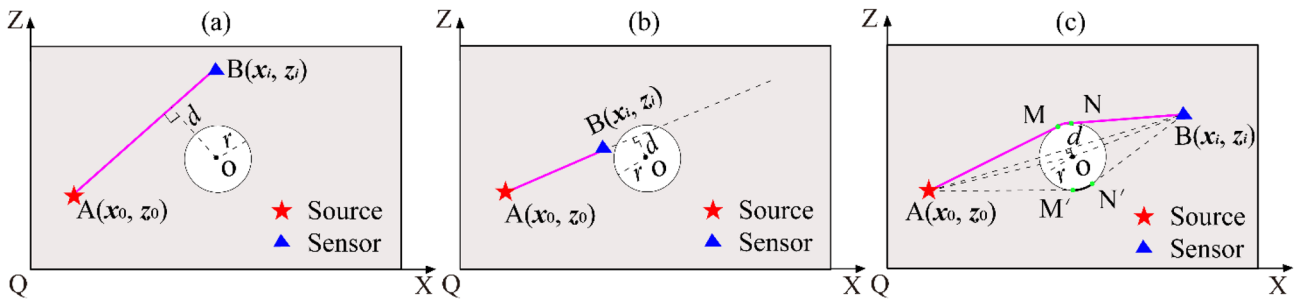

Fig. 1 Schematic diagrams of the shortest P-wave travel path in a 2D circle-contained rectangle. The red star and triangle denote the source and sensor locations, respectively. O is the circular center. d is the perpendicular distance from O to the line that connects A and B, r is the radius of the circular hole, M, M', N, and N' are tangent points

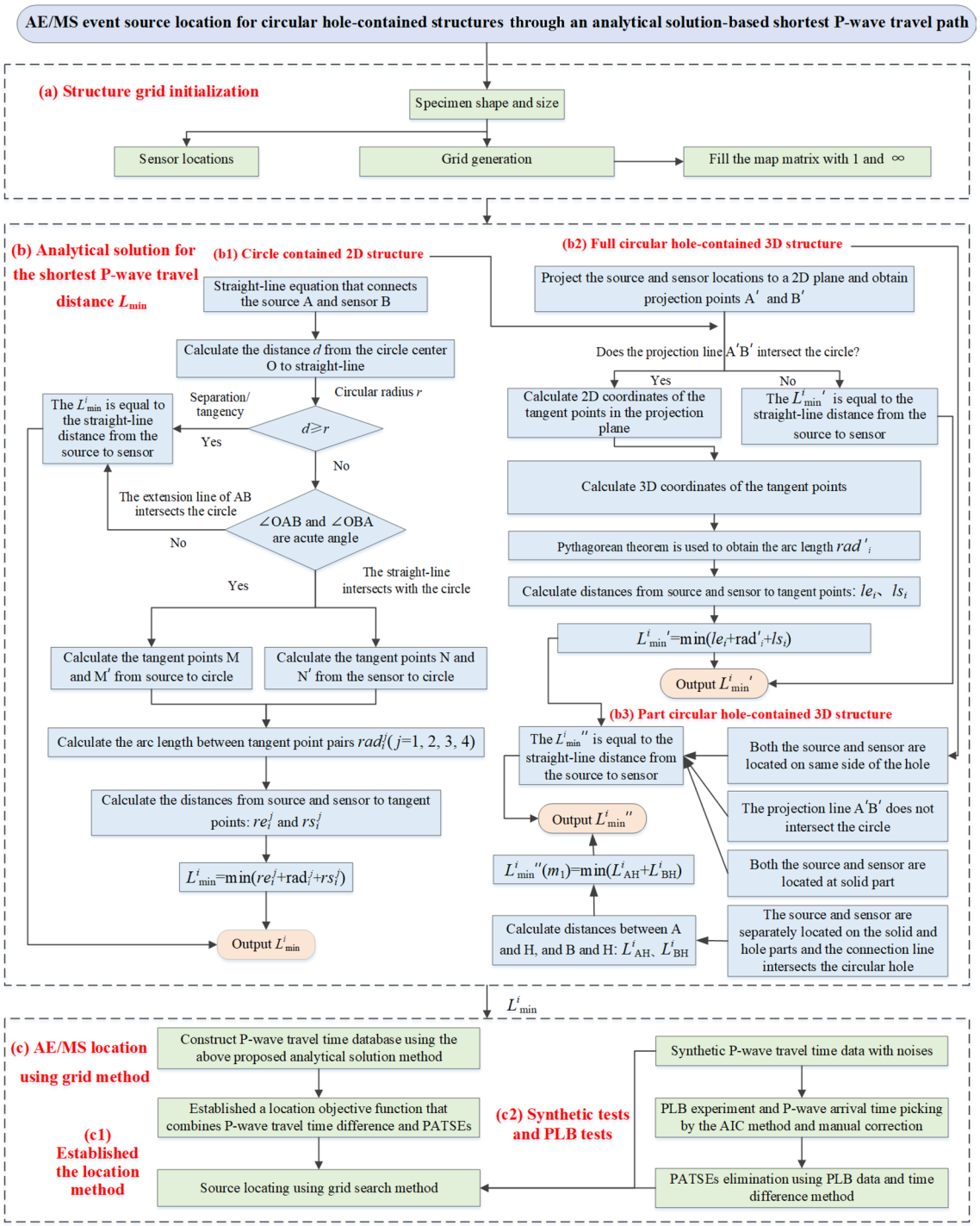

Fig. 2 Workflow of the analytical solution and proposed location method

AM+MN′+N′B, AM′+M′N′+N′B, and AM′+M′N+NB, and their corresponding arc lengths on the circle are marked as rad_i^j (j=1, 2, 3, 4).

$$rad_i^j = r\theta_j, \tag{7}$$

where $\theta_j = 2\arcsin\frac{d_q}{2r}$, $\theta_j \le 180°$ is the angle between the tangent points M, M', N, N' and the circular center O. $d_q = \sqrt{(xs_i - xe_i')^2 + (zs_i - ze_i')^2}$ indicates the straight line distance between tangent point combinations.

Mark the distance from the source to tangent points M and M' as le_i^j, and mark the distance from the sensor to tangent points N and N' as ls_i^j. The shortest P-wave travel path in a 2D circular hole-contained plane can be written as:

$$L_{\min}^i = \min(le_i^j + rad_i^j + ls_i^j). \tag{8}$$

2.1.2 Full Circular Hole-Contained 3D Structure

Set the source and sensor coordinates in the full circular hole-contained 3D structure separately as A(x_0, y_0, z_0) and B(x_i, y_i, z_i), where i is the sensor id. There also are three spatial relationships (separation, tangency, and intersection) between the connection line and the circular hole (Fig. 3). To identify this, the source and sensor locations are projected to the front plane of the full circular hole-contained 3D structure, and then the method proposed in Sect. 2.1.1 is used to judge the spatial relationship. The workflow detail is shown in Fig. 2b2.

The source and sensor locations in the projection plane are marked A′ (x_0, C, z_0) and B′ (x_i, C, z_i), respectively, where C is a constant equal to the Y-axis coordinate of the front plane. The perpendicular distance d' and spatial relationship between the connection line and circular hole can be obtained by following the steps shown in Sect. 2.1.1.

(a) If $d' \ge r$, the straight line is separated or tangent to the 3D full circular hole (Fig. 3d). The straight line distance from the source to the sensor is the shortest P-wave travel distance in the 3D space:

$$L'_{\min^i} = \sqrt{(x_i - x_0)^2 + (y_i - y_0)^2 + (z_i - z_0)^2}. \tag{9}$$

(b) If $d' < r$, the judgment method that whether the connection line or its extension line intersects the circular hole is the same as that shown in Sect. 2.1.1. If at least one of ∠OA′B′ and ∠OB′A′ is not an acute angle, the connection line does not pass through the circular hole (Fig. 3e), and Eq. (9) is used to calculate the $L'_{\min^i}$. Otherwise, the connection line passes through the circular hole (Fig. 3f), and the calculation method for $L'_{\min^i}$ is given as follows.

Set the tangent point coordinates from the source and station to the circular hole separately as G(xe_i, ye_i, ze_i) and

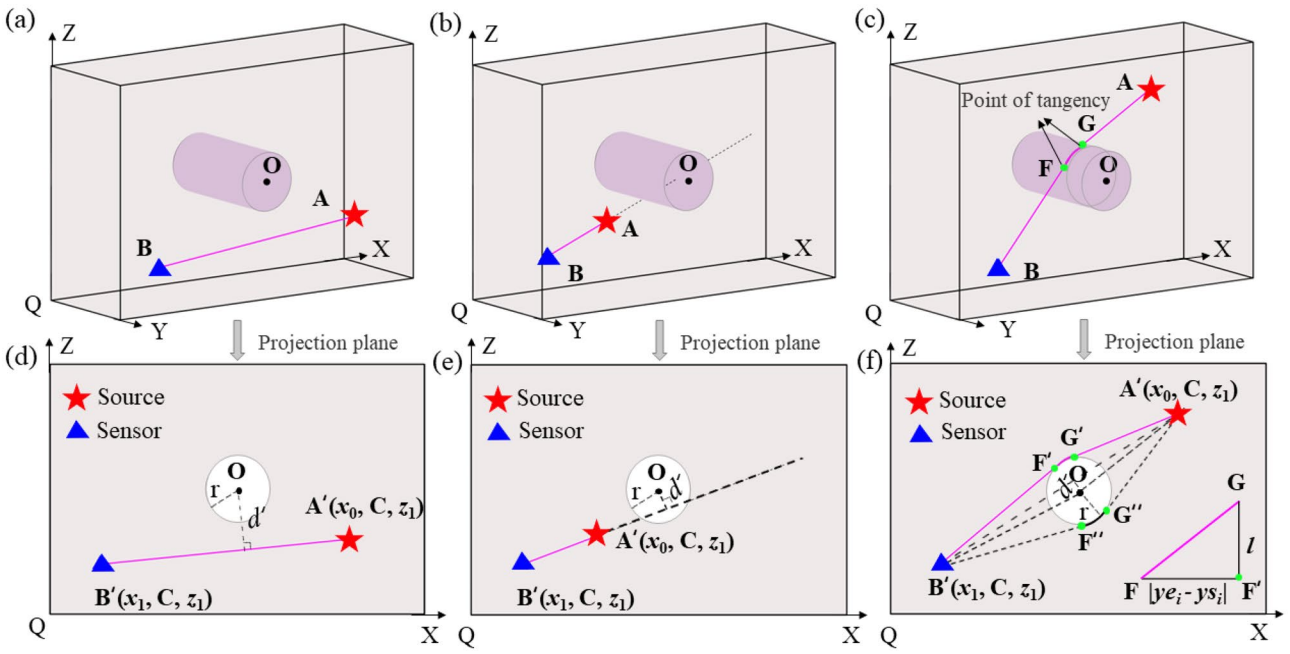

Fig. 3 Schematic diagrams of the shortest P-wave travel path in the full circular hole-contained 3D structure. The remaining description is the same as in Fig. 1

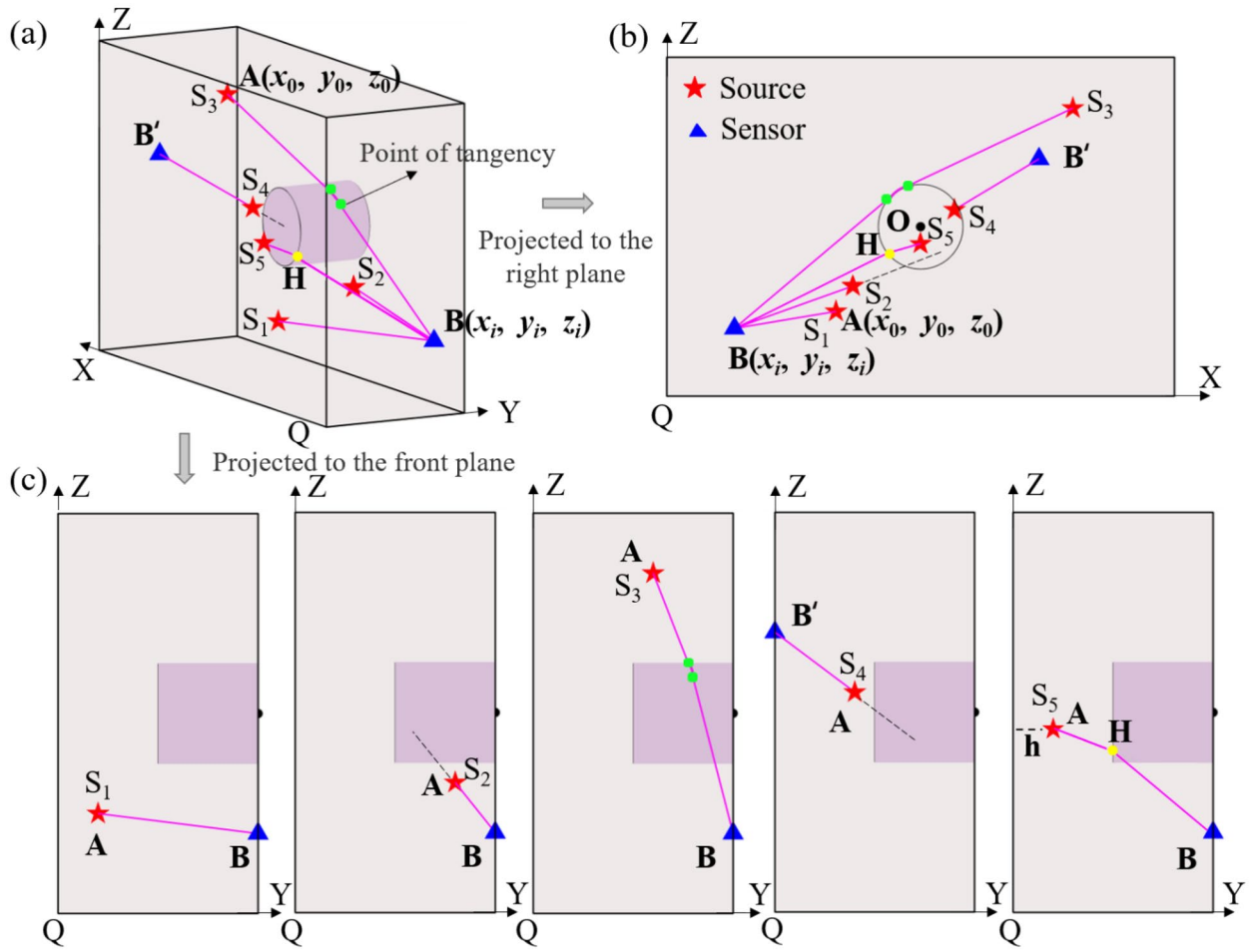

Fig. 4 Schematic diagrams of the shortest P-wave travel path in a part circular hole-contained 3D structure. **a** The part circular hole-contained 3D structure, source and sensor locations; **b–c** The source and sensors are projected to the right and front plane, respectively. The remaining description is the same as in Fig. 1

F(xs_i, ys_i, zs_i). There are six variables in the G and F, and the xe_i, ze_i, xs_i, and zs_i can be obtained by following the steps shown in Sect. 2.1.1, then only ye_i and ys_i are the unknown variables. The straight line distance le_i from the source to tangent point G and the straight line distance ls_i from station to tangent point F can be calculated by:

$$\begin{cases} le_i = \sqrt{(x_0 - xe_i)^2 + (y_0 - ye_i)^2 + (z_0 - ze_i)^2} \\ ls_i = \sqrt{(x_i - xs_i)^2 + (y_i - ys_i)^2 + (z_i - zs_i)^2} \end{cases}. \tag{10}$$

Moreover, to calculate the arc length rad_i' between tangent points, the G and F are projected to the front plane of the full circular hole-contained 3D structure, where the projected point coordinates are marked as G′(xe_i, C, ze_i) and F′(xs_i, C, zs_i). The circular hole is then expanded (Fig. 3f, a more visually 3D view has been included in Fig. S1 and the arc length l between the tangent points G′ and F′ in the 2D projected plane is obtained. FF′ is determined by the $|ye_i - ys_i|$, and mark the arc length between tangent points G and F in 3D space as rad_i'. The l, FF′ and rad_i' forms a triangle, and the rad_i' can be obtained according to Pythagorean theorem:

$$\mathrm{rad}_i' = \sqrt{(ye_i - ys_i)^2 + l^2}. \tag{11}$$

The l can be calculated in the same way as the rad_i^j shown in Sect. 2.1.1. $l = r\theta_1$ ($\theta_1 = 2\arcsin\frac{d_{G'F'}}{2r}$), where θ_1 is equal to $\angle$G′OF′, and $d_{G'F'} = \sqrt{(xs_i - xe_i)^2 + (zs_i - ze_i)^2}$ indicates the straight line distance between the G′ and F′.

Furthermore, the source, tangent points G and F, and sensor locations should be in the same plane $x + my + nz + e = 0$.

$$\begin{cases} x_0 + my_0 + nz_0 + e = 0 \\ xe_i + mye_i + nze_i + e = 0 \\ xs_i + mys_i + nzs_i + e = 0 \\ x_i + my_i + nz_i + e = 0 \end{cases}, \tag{12}$$

where m, n, and e are coefficients of the plane equation.

There are five unknown parameters in Eq. (12). The n, e, ye_i, and ys_i may then be expressed as a function of parameter m. Thus, the $L'_{\min^i}$ can be calculated by:

$$L'_{\min^i}(m) = \min(le_i + rad'_i + ls_i). \tag{13}$$

The partial derivative of parameter m can be used to solve Eq. (13):

$$\frac{\partial(le_i + \mathrm{rad}'_i + ls_i)}{\partial m} = 0. \tag{14}$$

After obtaining the parameter m, it is easy to obtain n, e, ye_i, and ys_i. Finally, the shortest P-wave travel distance will be $L'_{\min^i} = \min(le_i + \mathrm{rad}'_i + ls_i)$.

2.1.3 Part Circular Hole-Contained 3D Structure

Set the source and sensor coordinates in the part circular hole-contained 3D structure separately as A(x_0, y_0, z_0) and B(x_i, y_i, z_i), where i is the sensor id. In this case, there are five spatial relationships between the connection line and the circular hole (Fig. 4). The workflow detail is shown in Fig. 2b3:

(1) When the P-wave travel path is separated/tangent to the circular hole (e.g., straight lines S_1 and S_2 in Fig. 4, the spatial relationship can be determined by following Sect. 2.1.2), and the shortest P-wave travel distance $L''_{\min^i}$ can be calculated by Eq. (9).

(2) When the source and sensor are both located on the circular hole side (e.g., straight line S_3 in Fig. 4, the spatial relationship can be determined by the Y-axis coordinate), the shortest P-wave travel distance $L''_{\min^i}$ can be calculated by following the steps shown in Sect. 2.1.2.

(3) When the source and sensor are both located at the solid part (e.g., straight line S_4 in Fig. 4, the spatial relationship can be determined by the Y-axis coordinate), and the shortest P-wave travel distance $L''_{\min^i}$ can be calculated by Eq. (9).

(4) When the source and sensor are separately located on the solid and hole parts (e.g., straight line S_5 in Fig. 4, the spatial relationship can be determined by the Y-axis coordinates: the minimum value of y_0 and y_i is smaller than 5 cm, and the maximum value of y_0 and y_i is larger than 5 cm) and the connection line intersects the circular hole, the following steps are given to obtain the shortest P-wave travel distance:

The points A (x_0, y_0, z_0), H (xh_i, yh_i, zh_i), and B (x_i, y_i, z_i) on the P-wave path from the source to the sensor should be in the same plane $x + m_1y + n_1z + e_1 = 0$.

$$\begin{cases} x_0 + m_1y_0 + n_1z_0 + e_1 = 0 \\ xh_i + m_1yh_i + n_1zh_i + e_1 = 0 \\ x_i + m_1y_i + n_1z_i + e_1 = 0 \end{cases}. \tag{15}$$

Then, the point H should be on the circle of the front face and the yh_i is equal to the Y coordinate of the front face:

$$(x_c - xh_i)^2 + (z_c - zh_i)^2 = r^2, \tag{16}$$

$$yh_i = h. \tag{17}$$

The straight line distance between A and H is equal to $L^i_{\mathrm{AH}} = \sqrt{(x_0 - xh_i)^2 + (y_0 - yh_i)^2 + (z_0 - zh_i)^2}$, and the straight line distance between B and H is equal to $L^i_{\mathrm{BH}} = \sqrt{(x_1 - xh_i)^2 + (y_1 - yh_i)^2 + (z_1 - zh_i)^2}$. There are six unknown parameters in Eq. (15). Combining Eqs. (15)–(17), the n_1, e_1, xh_i, yh_i, and zh_i may then be expressed as a function of parameter m_1. Then, the length of shortest P-wave path from A to B can be written as:

$$L''_{\min^i}(m_1) = \min(L^i_{AH} + L^i_{BH}). \tag{18}$$

Table 1 Computation performance based on different grid sizes

Evaluation parameter	Circle-contained 2D rectangle (cm^2)			Full circular hole-contained 3D cuboid (cm^3)	
	1×1	0.5×0.5	0.25×0.25	2×2×2	1×1×1
Grid dataset generation time (h)	1.35	2.86	12.99	23.46	217.14
Grid search location time (s)	0.13	0.27	1.60	0.27	1.25
Average location error (cm)	0.49	0.57	0.56	4.96	1.87

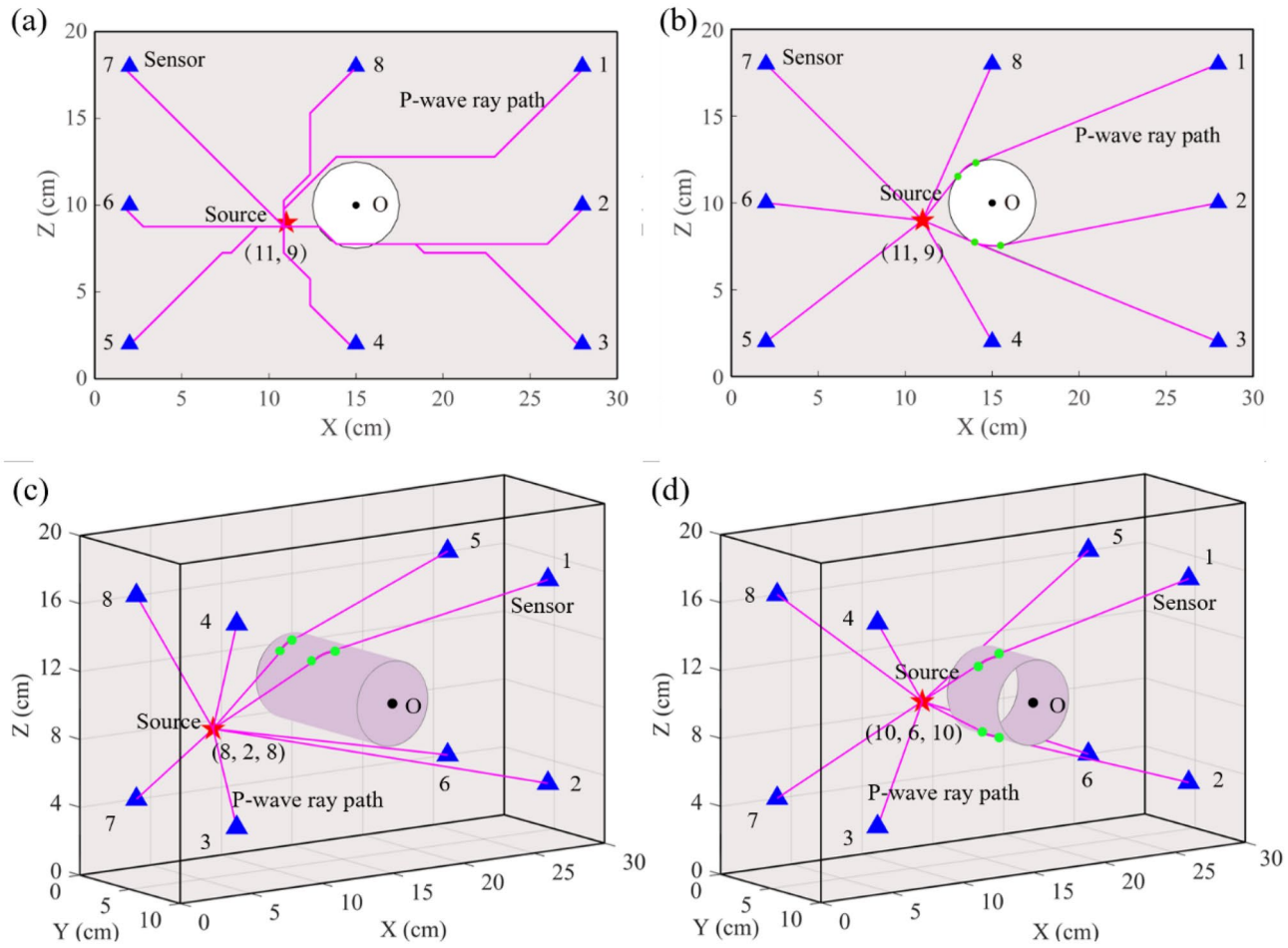

Fig. 5 Shortest P-wave travel paths from the sources to sensors. **a** Shortest P-wave travel paths obtained by the Dijkstra algorithm. **b–d** Shortest P-wave paths obtained by the proposed analytical solution for the circle-contained 2D rectangle, the full circular hole-contained 3D cuboid, and the part circular hole-contained 3D cuboid, respectively. The remaining description is the same as in Fig. 1

Table 2 Sensor locations on the circular hole-contained structures

The circle-contained 2D rectangle						The full/part circular hole-contained 3D cuboid							
Sensor id	Sensor location (cm)		Sensor id	Sensor location (cm)		Sensor id	Sensor location (cm)			Sensor id	Sensor location (cm)		
	x	*y*		*x*	*y*		*x*	*y*	*z*		*x*	*y*	*z*
1	28	18	5	2	2	1	26	10	16	5	26	0	16
2	28	10	6	2	10	2	26	10	4	6	26	0	4
3	28	2	7	2	18	3	4	10	4	7	4	0	4
4	15	2	8	15	18	4	4	10	16	8	4	0	16

The partial derivative of parameter m_1 can be used to solve Eq. (18):

$$\frac{\partial(L^i_{\mathrm{AH}}+L^i_{\mathrm{BH}})}{\partial m_1}=0. \tag{19}$$

After obtaining the parameter m_1, it is easy to obtain n_1, e_1, xh_i, and zh_i. Finally, the shortest P-wave travel distance will be $L''_{\min^i}=\min\left(L^i_{\mathrm{AH}}+L^i_{\mathrm{BH}}\right)$.

2.2 AE/MS Grid Search Location Method for Circular Hole-Contained Structure

The above analytical solution obtains an accurate P-wave travel time for the circular hole-contained structure. Then, it can be combined with the travel time-based source location objective function. In this study, an L1 norm time difference and PATSE combined objective function is proposed, and a grid search method is used to find the global optimal source location. The source location steps are shown in Fig. 2, and the detailed processes are listed as follows:

Step 1: structure grid initialization.

The circular hole-contained structure is divided into cubes, and their centers are used in the grid search-based source location method. In this study, the circular hole radius is 2.5 cm, the circular hole-contained rectangular has a size of 30×20 cm^2, the full and part circular hole-contained 3D cuboids both have a size of $30\times10\times20$ cm^3, and the hole length of the part circular hole-contained 3D cuboid is 5 cm. Evaluation parameters of circle-contained 2D rectangle and full circular hole-contained 3D cuboid listed in Table 1 were included to confirm the gird size, where all the parameters are based on one core of 2.8 GHz CPU and the application dataset shown in Sect. 5. For the circle-contained 2D rectangle, the 1×1, 0.5×0.5, and 0.25×0.25 cm^2 grids have a similar average location error, while the 0.25×0.25 cm^2 needs a much more grid dataset generation time and grid search location time. A 0.5×0.5 cm^2 grid is selected for circle-contained 2D rectangle. For the full circular hole-contained 3D cuboid, the average location error of the $2\times2\times2$ cm^3 grid is much larger than that based on the $1\times1\times1$ cm^3 grid. Computation performance based on $0.5\times0.5\times0.5$ cm^3 is not given in this study, due to that the grid generation time will be more than 1700 h, and the grid search location time will be more than 10 s, which is usually not acceptable for a real time source location. A $1\times1\times1$cm^3 grid is selected for circular hole-contained 3D cuboid. It should be mentioned that the grid dataset generation and grid search can be calculated in parallel, while for a laptop the above-selected grids are suggested.

Step 2: analytical solution for the shortest P-wave travel distance $L_{\min}$.

The analytical solution method proposed in Sect. 2.1 is used to calculate the P-wave travel distance from each grid to each sensor, and travel time datasets are generated for 2D circle-contained rectangle, 3D full circular hole-contained cuboid, and 3D part circular hole-contained cuboid, avoiding the repetitive calculation of travel time in each location.

Step3: AE/MS source location method for circular hole-contained structure.

The analytical solution is used as the input of the AE/MS source location. The AIC picking method and manual correction are then used to determine a good P-wave arrival time, and an example is shown in Sect. 4.2. The relatively PATSEs are obtained from location pre-measured PLB events.

Set the AE/MS occurrence time, picked P-wave arrival time, PATSE, and P-wave velocity as t_0, t_i, T_i, and v_p, respectively. Then, the relationship between P-wave travel time and travel distance can be established as:

$$L_{\min} = v_p(t_i - t_0 - T_i). \tag{20}$$

There are two unknown variables (t_0 and T_i) in Eq. (20). The t_0 can be eliminated by subtracting the Eq. (20) corresponding to the first sensor from the ith sensor, and it can also obtain the relative PATSE ($\Delta T_{i_1} = T_i - T_1 = t_i - t_1 - (L'_{\min^i} - L'_{\min^1})/v_p$) of the ith sensor. Therefore, the L1 norm time difference-based location objective function considering the PATSEs for circular hole-contained structures can be written as:

$$\text{Minimize } TFE = \sum_{i=1}^{n} \left| t_i - t_1 - \Delta T_{i1} - \frac{L^i_{\min}}{v_p} + \frac{L^1_{\min}}{v_p} \right|. \tag{21}$$

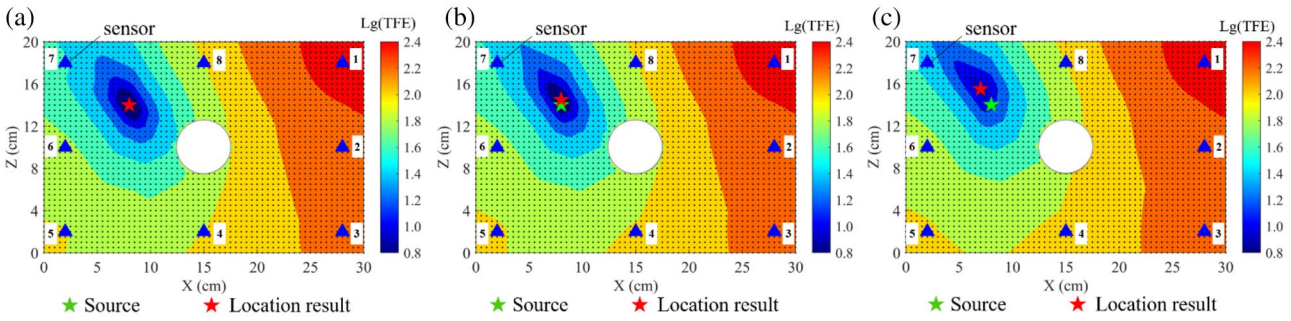

Fig. 6 Analytical solution-based synthetic location results for the circle-contained 2D structure. **a**–**c** Location results for noise-free, 1us Gaussian noises, and 2us Gaussian noises cases, respectively. The green and red five-pointed stars are the synthetic event location and location result, respectively (Color figure online)

Table 3 Location results of the synthetic events in circular hole-contained structures

Location method	Gaussian noises	Circle-contained 2D rectangle				Full circular hole-contained 3D cuboid					Part circular hole-contained 3D cuboid				
		X/cm	Y/cm	Min (TFE) /us	Error/cm	X/cm	Y/cm	Z/cm	Min (TFE) /us	Error /cm	X/cm	Y/cm	Z/cm	Min (TFE) /us	Error /cm
Analytical solution-based location method	0 us	8.0	14.0	0.0	0.0	8.5	4.5	8.5	0.0	0.0	9.5	4.5	14.5	0.0	0.0
	1 us	8.0	14.5	3.8	0.5	8.5	4.5	9.5	6.0	1.0	9.5	5.5	14.5	3.4	0.5
	2 us	7.0	15.5	8.5	1.8	8.5	6.5	8.5	8.3	2.0	10.5	4.5	16.5	12.6	2.2
Dijkstra algorithm-based location method	0 us	8.5	14.0	2.9	0.5	8.5	3.5	6.0	66.1	2.7	4.5	4.5	16.0	57.1	12.5
	1 us	9.0	14.0	4.8	1.0	8.5	3.5	6.0	64.3	2.7	5.5	4.5	16.0	56.3	11.5
	2 us	9.0	15.5	11.8	1.8	9.5	3.5	6.0	62.5	2.9	4.5	4.5	16.0	61.4	12.5

When locating an AE/MS event, a *TFE* can be obtained for each grid, and the grid with a minimum *TFE* value is taken as the source location result.

3 Synthetic Tests

To verify the effectiveness of the AE/MS location method proposed in Sect. 2, a circle-contained 2D rectangle (30×20 cm^2), a full circular hole-contained 3D cuboid ($30 \times 10 \times 20$ cm^3), and a part circular hole-contained 3D cuboid ($30 \times 10 \times 20$ cm^3) were selected to carry out the synthetic tests (Fig. 5b–d). The measured P-wave velocity 0.6 cm/us is adopted. The sensor locations are listed in Table 2. The circular hole ($r = 2.5$ cm) is set in the structure centers. The hole length of the part circular hole-contained 3D cuboid is 5 cm.

3.1 Computation Example of the Shortest Path

The source locations coordinates (11, 9) cm, (8, 2, 8) cm, and (10, 6, 10) cm are selected for the circle-contained 2D rectangle, the full circular hole-contained 3D cuboid, and the part circular hole-contained 3D cuboid, respectively. The analytical solution-based shortest P-wave travel paths are shown in Fig. 5b–d. The Dijkstra algorithm-based shortest P-wave travel paths of the circle-contained 2D rectangle (Fig. 5a) are also offered for comparison. It should be noted that the Dijkstra algorithm has an extremely poor optimal P-wave travel path for 3D structures, which is not shown here. The analytical solution-based shortest P-wave travel path usually has fewer turning points than the Dijkstra algorithm (Fig. 5a, b). The P-wave signal travels along the circular arc when the connection line intersects the circular hole (Fig. 5b, c and d), which demonstrates the superiority of the proposed analytical solution in finding the shortest P-wave travel path.

3.2 Synthetic Tests for the Circle-Contained 2D Rectangle

First, the theoretical P-wave travel time dataset was generated by the proposed method in Sect. 2.1.1. Since the recorded P-wave arrival data may contain errors due to background noise, Gaussian noise with a mean value of 0 and standard deviations of 1 us and 2 us were added to the theoretical P-wave travel time dataset. The grid search algorithm-based location results for the circle-contained 2D structure are shown in Fig. 6. There is a small time fitting error (TFE) near the source, and the location errors are 0 cm, 0.5 cm, and 1.8 cm for the noise-free, 1us Gaussian noise, and 2us Gaussian noise cases, respectively (Table 3). Moreover, location results based on the P-wave travel path

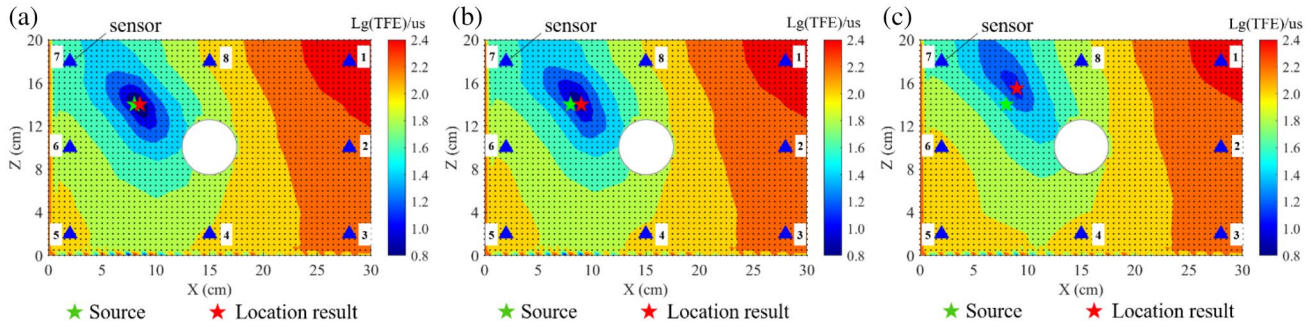

Fig. 7 Dijkstra algorithm-based synthetic location results for the circle-contained 2D structure. The remaining description is the same as in Fig. 6

Table 4 TFE log statistics in the zone 3.5 cm ≤ X ≤ 12.5 cm and 10 cm ≤ Z ≤ 20 cm

Evaluation parameter	The proposed method			Dijkstra method		
	Noise free	1 us	2 us	Noise free	1 us	2 us
Variance	0.05	0.05	0.05	0.05	0.04	0.04
Standard variance	0.23	0.23	0.22	0.22	0.20	0.19
Mean	1.46	1.46	1.49	1.51	1.52	1.57
Median	1.48	1.48	1.52	1.54	1.54	1.57

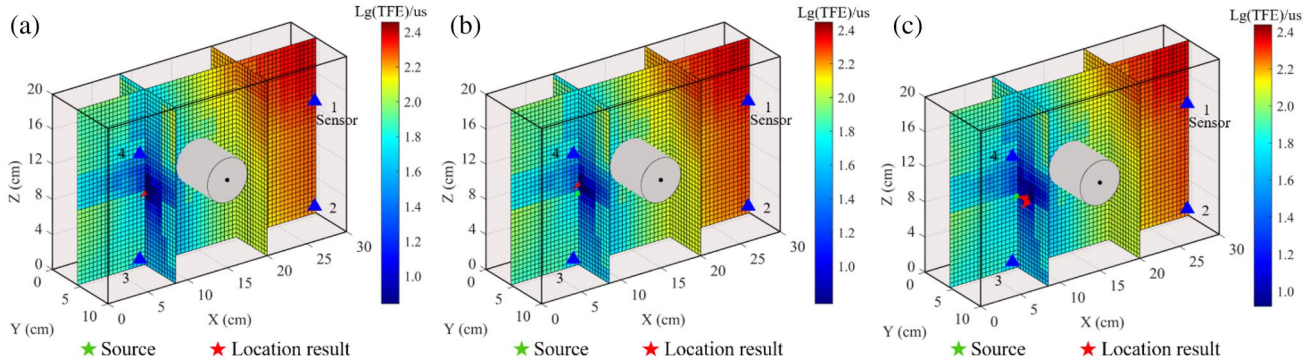

Fig. 8 Analytical solution-based synthetic location results for the full circular hole-contained 3D cuboid. The remaining description is the same as in Fig. 6

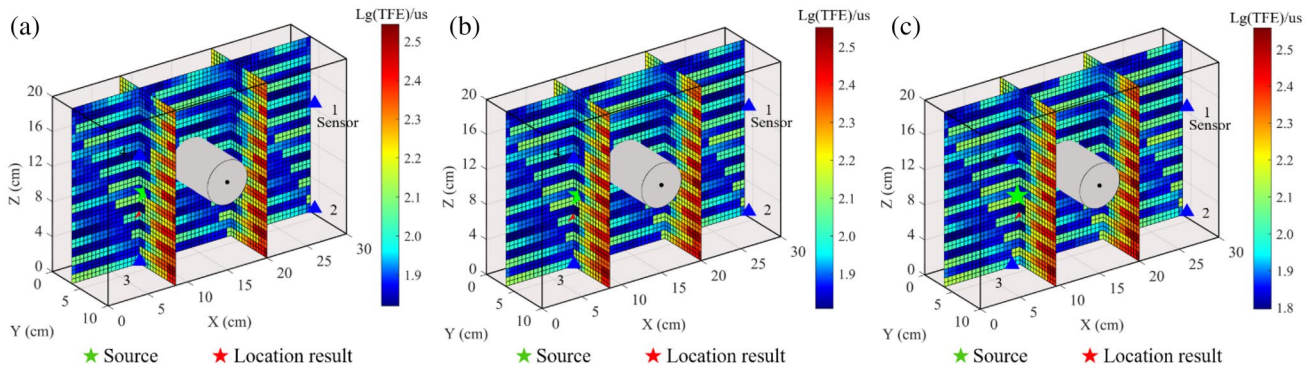

Fig. 9 Dijkstra algorithm-based synthetic location results for the full circular hole-contained 3D cuboid. The remaining description is the same as in Fig. 6

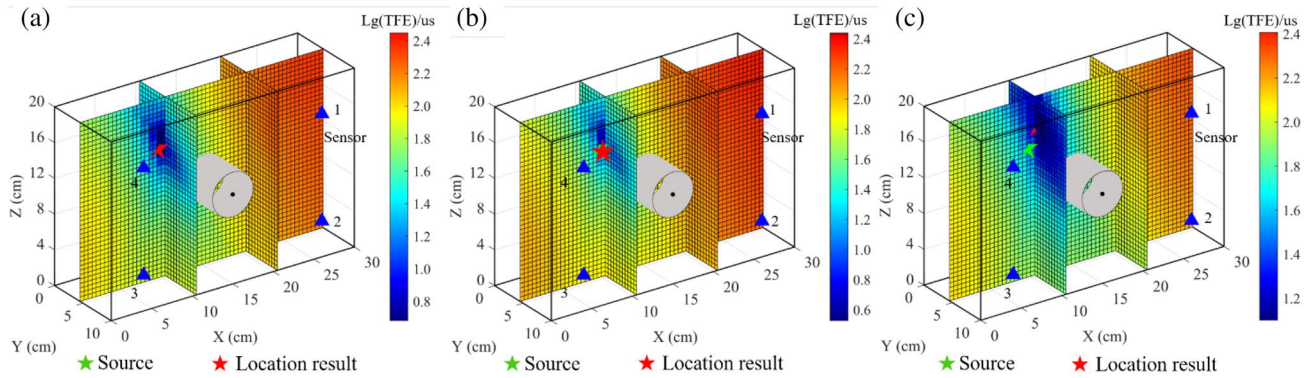

Fig. 10 Analytical solution-based synthetic location results for the part circular hole-contained 3D cuboid. The remaining description is the same as in Fig. 6

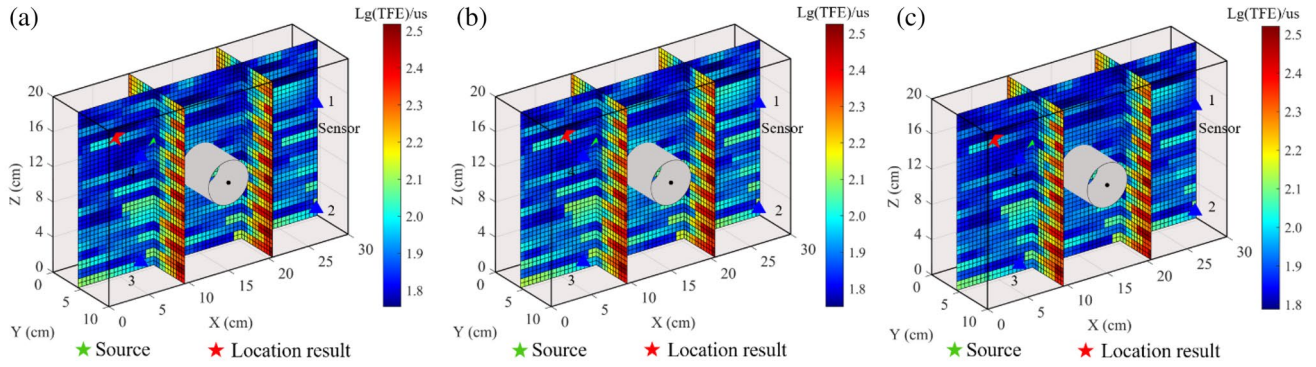

Fig. 11 Dijkstra algorithm-based synthetic location results for the part circular hole-contained 3D cuboid. The remaining description is the same as in Fig. 6

of the Dijkstra algorithm (Fig. 7) are selected for comparison. It is clear that the new method has a smaller time fitting error (TFE) than that of the Dijkstra method. Moreover, the TFE log statistics in the zone 3.5 cm $\leq$ X $\leq$ 12.5 cm and 10 cm $\leq$ Z $\leq$ 20 cm near the true source location are listed in Table 4. It can be seen that the Dijkstra method may have a smaller variance and standard variance than the proposed method, which means that the Dijkstra method has a more stable TFE. On the other hand, the mean and median value of the proposed method is smaller than that of the Dijkstra method, which means the proposed method obtained better time fitness. The location errors based on the Dijkstra algorithm are 0.5 cm, 1.0 cm, and 1.8 cm for the noise-free, 1us Gaussian noise, and 2us Gaussian noise cases, respectively, which indicate that the proposed method obtains a good P-wave travel path.

It can be seen that the location accuracy will decrease with the increase of random noise. For an AE/MS source location, we tried to minimize the difference between theoretical data and observed data, and better theoretical data usually corresponds to better location results. Here, the theoretical data correspond to the data generated by the new method and Dijkstra method. The results shown in Fig. 5 demonstrate that the new method can generate a better P-wave travel time dataset than that of the Dijkstra method. Therefore, as the noise increases, the new method will still be better than the Dijkstra method. For large noises, both the new method and Dijkstra method will fail in the source location. It should be mentioned that better theoretical data may obtain a worse result, due to the effects of observed data noise and the inversion method.

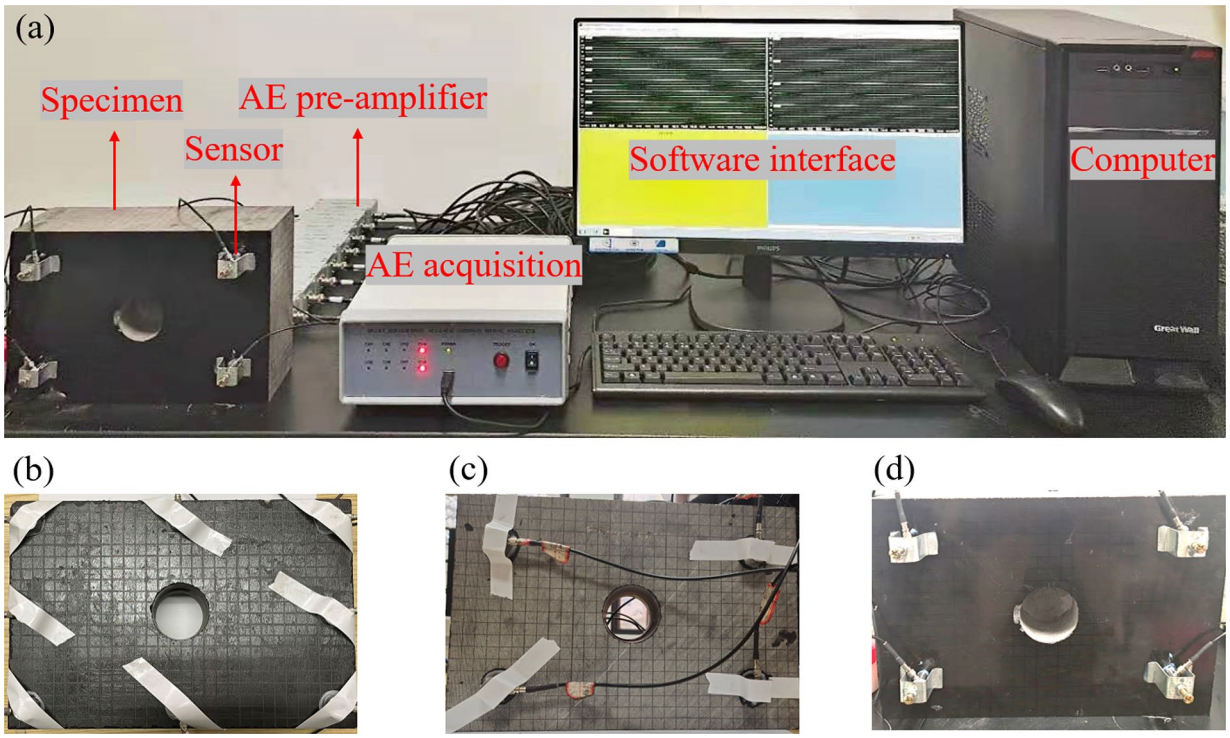

Fig. 12 AE experiment equipment and sensor layout. **a** AE monitoring system. **b–d** Sensor layout for the circle-contained 2D rectangle, the full circular hole-contained 3D cuboid, and the part circular hole-contained 3D cuboid, respectively

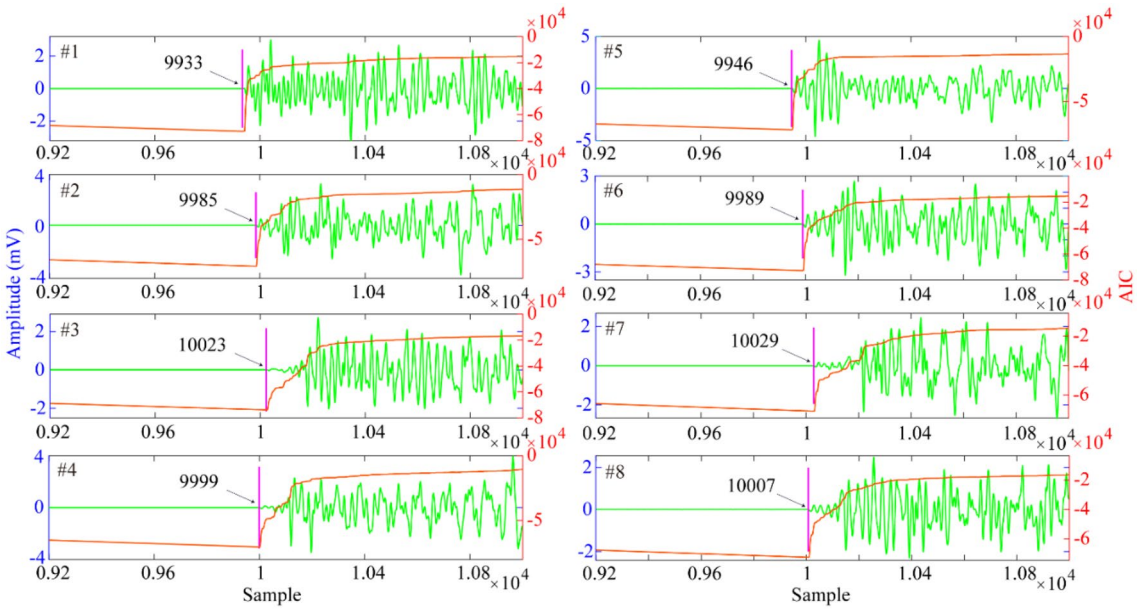

Fig. 13 PLB event waveforms and P-wave arrival picking results. The green and red curves correspond to the waveforms and the AIC time series, respectively. The number indicated by an arrow shows the AIC picking result. The # in the upper left corner indicates the sensor ID (Color figure online)

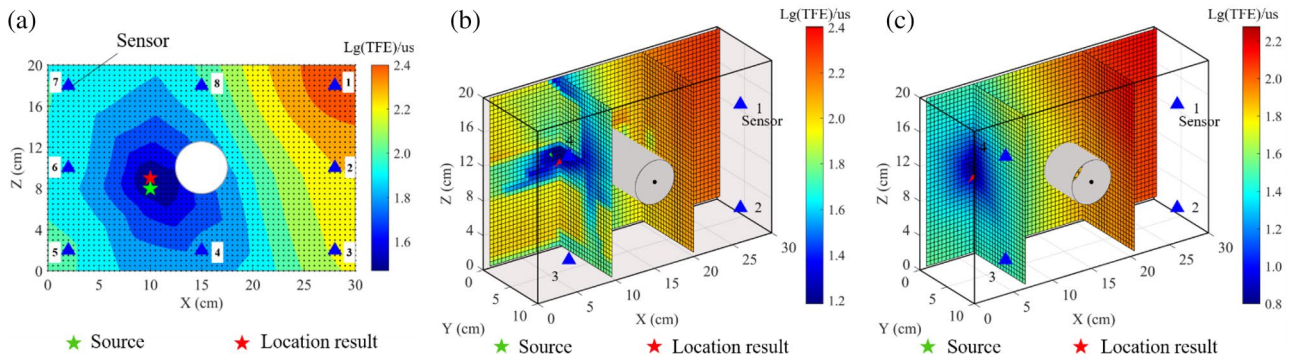

Fig. 14 Location results of three typical PLB events. **a–c** Location results of the circle-contained 2D structure, the full circular hole-contained 3D cuboid, and the part circular hole-contained 3D cuboid, respectively. The remaining description is the same as in Fig. 6

3.3 Synthetic Tests for the Circular Hole-Contained 3D Cuboid

The analytical solutions proposed in Sects. 2.1.2 and 2.1.3 are used to generate theoretical P-wave travel time for the full circular hole-contained 3D cuboid and part circular hole-contained 3D cuboid. The proposed location method in Sect. 2.2 is adopted to obtain Fig. 8 for the full circular hole-contained 3D cuboid. The small TFE areas concentrate around the synthetic event, and the location errors are less than 2 cm even when 2 us Gaussian noises were included. Following the same approach, the Dijkstra algorithm-based location results are shown in Fig. 9 for comparison. The Dijkstra algorithm-based TFE is much larger than that of our proposed method. It appears that Dijkstra algorithm-based TFE has a random distribution, and its location errors are all larger than 2 cm.

Location results of the analytical solution method and Dijkstra algorithm for the part circular hole-contained 3D cuboid are shown in Figs. 10 and 11, respectively. There is a TFE focusing area for the analytical solution method. However, the TFE is a bit larger than that of Fig. 8, which may be caused by sensor number reduction. For the 2us Gaussian noise, the analytical solution-based location error is 2.2 cm, while the Dijkstra algorithm-based location error reaches 12.5 cm. Moreover, the Dijkstra algorithm-based location has poor time fitting. In sum, the proposed location method has a good location accuracy and stability for circular hole-contained structures.

4 Experiment Tests

4.1 Experimental Setup

To further verify the location performance of the proposed method, three pieces of granite specimens (Fig. 12b–d) with the same size as those shown in Fig. 5 are used to conduct the PLB experiments, and the experiment was conducted using a DS5-8A acoustic emission monitoring device (Fig. 12a). The measured P-wave velocity is 6000 m/s, and the sensor layout for the circle-contained 2D rectangle, full circular hole-contained 3D cuboid, and part circular hole-contained 3D cuboid are shown in Fig. 12b–d, respectively. The sensor locations are the same as in Table 2, and all the sensors have a sampling frequency of 3 MHz. The AE pre-amplifiers are all set to 40 dB. The surfaces of these three granite specimens were divided into 1×1 cm^2 grids for PLB tests.

4.2 Experiment Data Processing

PLB events were conducted at the grid intersection points. However, there are no PLB events for some grid intersection points due to the sensor layout, sensor sensitivity and signal energy. It should be mentioned that the PLB events with less than seven sensors are not considered in the location. The monitored typical PLB signals and calculated AIC time series are shown in Fig. 13, where the AIC time series is based on the Sleeman and van Eck (1999). The AIC picking corresponds to the point with the minimum AIC value. The AIC method can usually obtain a good P-wave arrival picking. However, it can be affected by noise and signal tails. In this case, manual picking will be used to correct the P-wave arrival picking. Furthermore, 30 PLB events were used to obtain a series of relatively PATSEs ΔT_{i1}, and the median value is taken as the ΔT_{i1} of the ith sensor. Then, the source location can be conducted using Eq. (21).

5 Results and Discussion

5.1 Location Results of Typical PLB Events

Typical PLB event locations (10, 8), (8, 0, 12), and (10, 0, 10) cm were selected for further testing of the

Table 5 Location results of three typical PLB events

Location method	Circle-contained 2D rectangle				Full circular hole-contained 3D cuboid				Part circular hole-contained 3D cuboid			
	X/cm	Y/cm	Min (TFE)/us	Error/cm	X/cm	Y/cm	Z/cm	Min (TFE)/us	Error/cm	X/cm	Y/cm	Z/cm	Min (TFE)/us	Error/cm
Analytical solution-based location method	10.0	9.0	29.4	1.0	9.5	0.5	10.5	15.3	2.2	6.5	0.5	9.5	6.1	3.6
Dijkstra algorithm-based location method method	11.0	8.5	30.0	1.1	8.5	2.5	15.5	50.2	4.3	27.5	3.5	6.5	44.6	18.2

circle-contained 2D rectangle, the full circular hole-contained 3D cuboid, and the part circular hole-contained 3D cuboid, respectively. The location results are shown in Fig. 14 and Table 5. It is easy to see that the analytical solution-based location method obtains good TFE convergence for the PLB events, and the location errors of these three PLB events are 1.0 cm, 2.2 cm, and 3.6 cm, respectively. By contrast, the location errors of the Dijkstra algorithm are 1.1 cm, 4.3 cm, and 18.2 cm, respectively. This also demonstrates that the proposed method is better than the Dijkstra algorithm in finding the shortest P-wave travel path.

5.2 PLB Event Application

The proposed method has been applied to locate all the PLB events, and the location results are shown in Figs. 15, 16, 17 for the circle-contained 2D structure, the full circular hole-contained 3D cuboid, and the part circular hole-contained 3D cuboid, respectively. The line connects the PLB event and its location result: the longer the connection line, the larger the location error. The proposed method obtains good location results for all the circular hole-contained structures: the average location errors of these three specimens are 0.57 cm, 1.87 cm, and 2.25 cm, respectively. The location errors may come from P-wave arrival error. Then, Liu et al. (2022) showed that the PATSEs might be a time-dependent parameter. Thus a constant PATSE value will reduce the location accuracy.

Furthermore, the location errors of the analytical solution, straight line, Dijkstra and A* algorithms-based location methods are shown in Fig. 18. It can be seen that the proposed location method obtains a smallest average location error for these three circular hole-contained structures. For the circle-contained 2D structure, all the four methods obtain good location results. This is because the Dijkstra and A* algorithms have a good shortest P-wave travel path search performance with simple structures. For 3D structures, the analytical solution-based location results are much better than those based on the Dijkstra algorithm. The Dijkstra algorithm-based location results show a random distribution compared with cuboid size, which indicates that Dijkstra algorithm has a limited shortest path search ability for complex structures. The A* algorithm has a relatively good search ability for complex structures, an example is shown in Fig. S2. However, it may still obtain an optimal local path, and its grid search procedure may generate a small deviation between the search path and the actual shortest path, which reduces the location accuracy. It should be mentioned that the straight based location method obtains a good location accuracy, which is a result that the circular hole is small in this study.

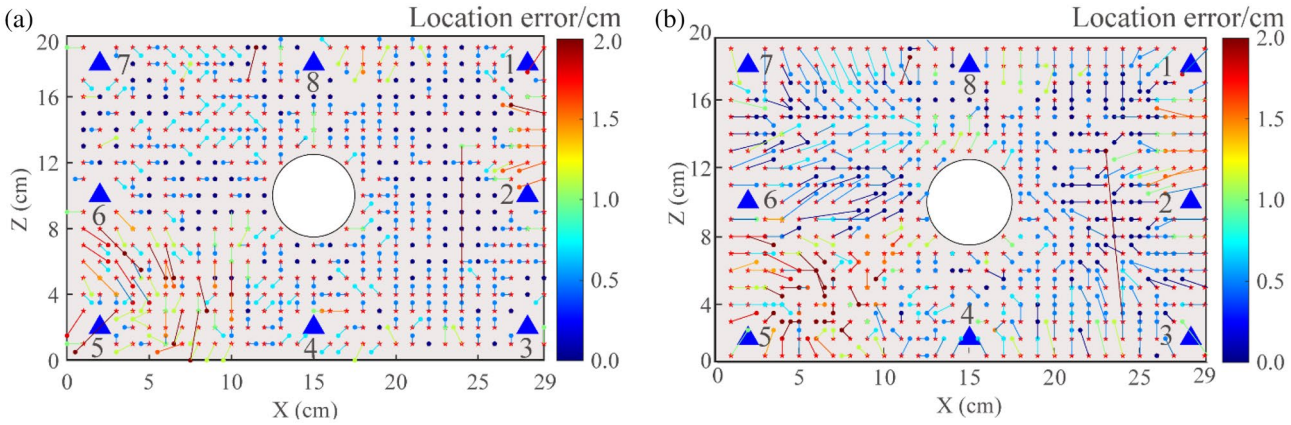

Fig. 15 PLB event location results for the circle-contained 2D structure. **a**, **b** Location results using the analytical solution- and the Dijkstra algorithm-based location methods, respectively. The data of **b** come from Zheng et al. (2022). The blue triangles and the red five-pointed stars represent sensor and PLB event locations, respectively. The dots are the location results, the dot color represents its location error, and the line connects the PLB event and its location result

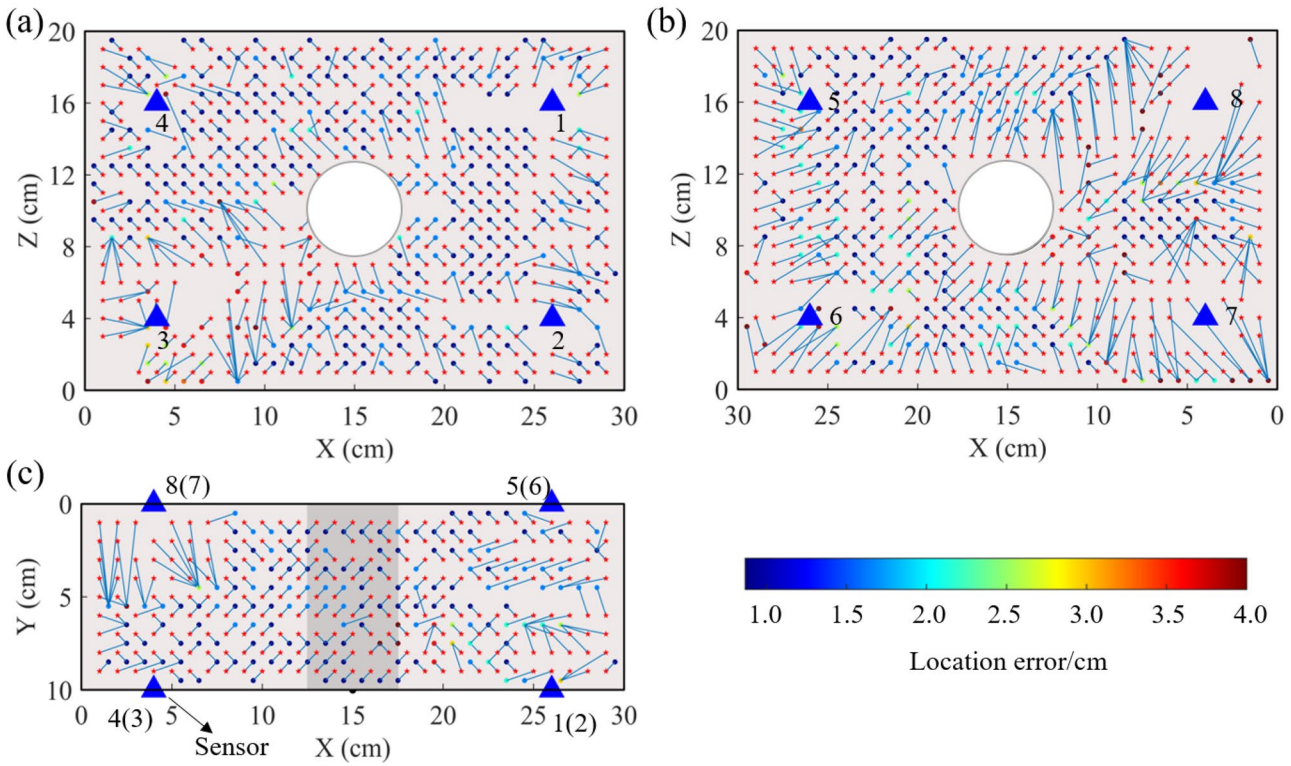

Fig. 16 PLB event location results for the full circular hole-contained 3D cuboid. **a–c** Location results of PLB events on the cuboid's front, back, and top surfaces, respectively. The remaining description is the same as in Fig. 15

5.3 Potential Studies

The above results demonstrate the effectiveness of the analytical solution-based P-wave shortest path for circular hole-contained structures. Moreover, the analytical solution-based P-wave travel time can be combined with various inversion methods (e.g., Newton iteration and Bayesian inversion (Shang and Tkalčić 2020)) to solve the source location objective function. The traditional pipeline location

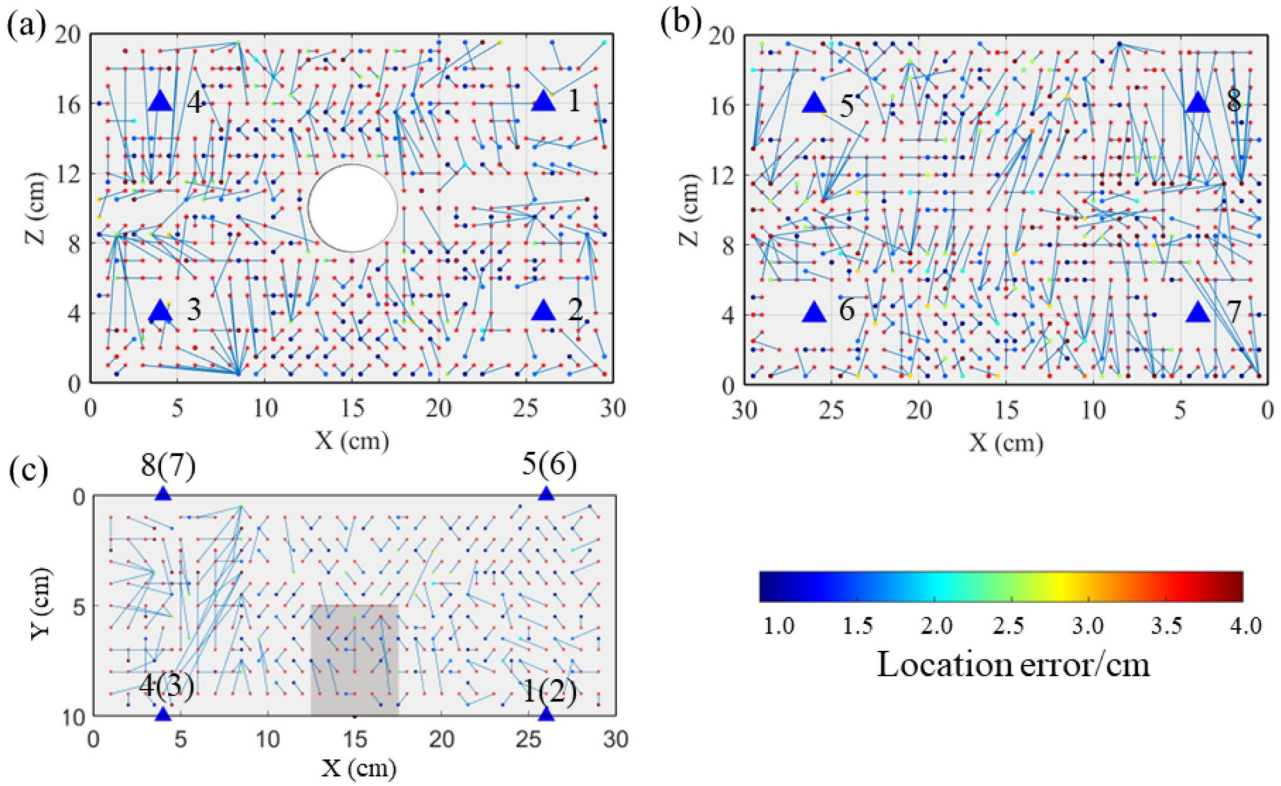

Fig. 17 PLB event location results for the part circular hole-contained 3D cuboid. The remaining description is the same as in Fig. 16

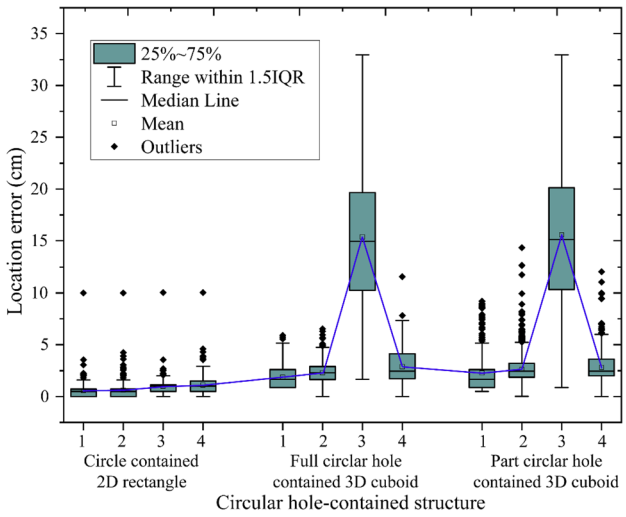

Fig. 18 Location errors of all the PLB events. The number 1, 2, 3, and 4 in each boxplot group correspond to the location errors of the analytical solution, straight line, Dijkstra and A* algorithm-based location methods, respectively

methods ignore the thickness of the pipelines (Dehghan Niri et al. 2015), which will increase the location error, especially for pipelines with a small circular diameter. By contrast, the proposed solution can consider the pipeline thickness, and it will improve the AE location accuracy of a pipeline structure. To date, many grid search-based algorithms have been applied to find the shortest P-wave travel path, such as the Dijkstra and A*. However, these methods may obtain optimal local paths (e.g., Fig. 8 in (Dong et al. 2020)). In this study, the rock specimens are treated as a homogenous material, however, there are many joints in an engineering scale and resulting in velocity differences in different directions. For example, the P-wave velocity in an engineering tunnel shows a strong heterogeneity (Wang et al. 2018). The homogeneous velocity model (e.g., Li et al. 2016) is still the most frequently used one, where treating the velocity model as a constant variable (e.g., Dong et al. 2019) is a special case. Results show that the homogeneous velocity model can obtain an acceptable location error (average location error is about 40 m). To handle this, some researchers used 1D velocity model (e.g., Feng et al. 2015b) and 3D velocity model (e.g., Wang et al. 2020) for MS source location, which improved the location result (average location error is about 20 m). A more accurate location result can consider a higher resolution 3D velocity model and signal attenuation. Moreover, the proposed method cannot be applied to projects with complex and diverse sections at this stage. The analytical solution for a project that has a cuboid or arched

section may be derived by following similar steps. However, for a project that has a diverse section, searching algorithms (e.g., Dijkstra and A* algorithms) may be adopted. In addition, For an engineering project (e.g., a mine) with the hole much smaller than the project, the influence of the hole on the wave arrival time will be relatively small, which may be negligible. While for a mining tunnel, pipelines, and pressure vessels, the hole will have a relatively large influence on the wave arrival time. In this study, we focused on the later research background.

6 Conclusions

The commonly used straight line, Dijkstra, and A* search algorithms are challenging to locate AE/MS events for circular hole-contained structures. To handle this, an analytical solution of the shortest P-wave travel path and a double difference and PATSE combined location objective function were proposed in this study. Then, comprehensive synthetic tests and PLB application tests were conducted to verify the proposed method. The main conclusions are given as follows:

(1) An analytical solution of the shortest P-wave travel path has been derived for the circle-contained 2D structure, the full circular hole-contained 3D cuboid, and the part circular hole-contained 3D cuboid, which can ensure an accurate P-wave travel time for circular hole-contained structures.
(2) An accurate P-wave travel time dataset is generated by the proposed analytical solution method. Then a time difference and PATSE combined source location objective function is established. The analytical solution-based location method has a good time fitting error convergence for the synthetic tests and the PLB events: the average location errors of the PLB events are 0.57 cm, 1.87 cm, and 2.25 cm for the circle-contained 2D structure, the full circular hole-contained 3D cuboid, and the part circular hole-contained 3D cuboid, respectively.
(3) For the circular hole-contained 3D structure, the location results of the analytical solution-based location method are much better than those based on the Dijkstra algorithm. The analytical solution can effectively overcome the problem of the search algorithm obtaining a locally optimal P-wave path. Furthermore, unlike the Dijkstra and A* search algorithms, there will be no gridding error with the analytical solution method.

Supplementary Information The online version contains supplementary material available at https://doi.org/10.1007/s00603-023-03227-0.

Acknowledgements The authors gratefully acknowledge the financial support of the National Natural Science Foundation of China under Grants 52004041 and U21A2030, the State Key Laboratory of Coal Mine Disaster Dynamics and Control (2011DA105287-MS202108), the Key Natural Science Foundation Project of Chongqing (cstc2020jcyj-zdxmX0023).

Author Contributions XS acquired methodology, software, conceptualization, provided resources and revision. CL acquired writing—original draft. XL acquired supervision and revision. LH acquired revision.

Data availability The acoustic emission data are available by contacting the corresponding author.

Declarations

Conflict of Interest The authors declare that they have no conflicts of interest to this work.

References

Baxter MG, Pullin R, Holford KM, Evans SL (2007) Delta T source location for acoustic emission. Mech Syst Signal Process 21(3):1512–1520

Dehghan Niri E, Farhidzadeh A, Salamone S (2015) Determination of the probability zone for acoustic emission source location in cylindrical shell structures. Mech Syst Signal Process 60–61:971–985

Dong L, Li X, Zhou Z et al (2015) Three-dimensional analytical solution of acoustic emission source location for cuboid monitoring network without pre-measured wave velocity. Trans Nonferrous Metals Soc China 25(1):293–302

Dong L, Zou W, Li X et al (2019) Collaborative localization method using analytical and iterative solutions for microseismic/acoustic emission sources in the rockmass structure for underground mining. Eng Fract Mech 210:95–112

Dong L, Hu Q, Tong X, Liu Y (2020) Velocity-free MS/AE source location method for three-dimensional hole-containing structures. Engineering 6(7):827–834

Dong L, Tao Q, Hu Q et al (2022) Acoustic emission source location method and experimental verification for structures containing unknown empty areas. Int J Min Sci Technol 32(3):487–497

Feng GL, Feng XT, Chen B et al (2015a) A microseismic method for dynamic warning of rockburst development processes in tunnels. Rock Mech Rock Eng 48(5):2061–2076

Feng GL, Feng XT, Chen BR et al (2015b) Sectional velocity model for microseismic source location in tunnels. Tunn Undergr Space Technol 45:73–83

Gesret A, Desassis N, Noble M et al (2015) Propagation of the velocity model uncertainties to the seismic event location. Geophys J Int 200(1):52–66

Hu Q, Dong L (2020) Acoustic emission source location and experimental verification for two-dimensional irregular complex structure. IEEE Sensors J 20(5):2679–2691

Jiang C, Liu C, Shang X (2021a) Double event joint location method considering P-wave arrival time system errors. Soil Dyn Earthq Eng 149:106890

Jiang R, Dai F, Liu Y, Li A (2021b) Fast marching method for microseismic source location in cavern-containing rockmass: performance analysis and engineering application. Engineering 7(7):1023–1034

Koabaz M, Hajzargarbashi T, Kundu T, Deschamps M (2012) Locating the acoustic source in an anisotropic plate. Struct Health Monit 11(3):315–323

Kundu T, Nakatani H, Takeda N (2012) Acoustic source localization in anisotropic plates. Ultrasonics 52(6):740–746

Li XB, Wang ZW, Dong LJ (2016) Locating single-point sources from arrival times containing large picking errors (LPEs): the virtual field optimization method (VFOM). Sci Rep 6:19205

Liu C, Shang X, Miao R (2022) Acoustic emission source location on a cylindrical shell structure through grouped sensors based analytical solution and data field theory. Appl Acoust 192:108747

Mborah C, Ge M (2018) Enhancing manual P -phase arrival detection and automatic onset time picking in a noisy microseismic data in underground mines. Int J Min Sci Technol 28(4):691–699

Peng P, Jiang Y, Wang L, He Z (2020) Microseismic event location by considering the influence of the empty area in an excavated tunnel. Sensors 20(2):574

Peng K, Guo H, Shang X (2021) EEMD and multiscale PCA-based signal denoising method and its application to seismic P-phase arrival picking. Sensors 21(16):5271

Peng K, Guo H, Shang X (2022) Microseismic source location using the log-cosh function and distant sensor-removed P-wave arrival data. J Cent South Univ 29(2):712–725

Rui Y, Zhou Z, Lu J et al (2022) A novel AE source localization method using clustering detection to eliminate abnormal arrivals. Int J Min Sci Technol 32(1):51–62

Shang X, Li X, Morales-Esteban A, Dong L (2018) Enhancing microseismic P-phase arrival picking: EMD-cosine function-based denoising with an application to the AIC picker. J Appl Geophys 150:325–337

Shang X, Wang Y, Miao R (2022) Acoustic emission source location from P-wave arrival time corrected data and virtual field optimization method. Mech Syst Signal Process 163:108129

Shang X, Tkalčić H (2020) Point-source inversion of small and moderate earthquakes from P-wave polarities and P/S amplitude ratios within a hierarchical Bayesian framework: implications for the geysers earthquakes. J Geophys Res Solid Earth 125:e2019JB018492

Sleeman R, van Eck T (1999) Robust automatic P-phase picking: an on-line implementation in the analysis of broadband seismogram recordings. Phys Earth Planet Inter 113(1–4):265–275

Wang Z, Li X, Zhao D et al (2018) Time-lapse seismic tomography of an underground mining zone. Int J Rock Mech Min Sci 107:136–149

Wang Y, Shang X, Peng K (2020) Locating mine microseismic events in a 3D velocity model through the Gaussian beam reverse-time migration technique. Sensors 20:2676

Wang S, Wang H, Wang D et al (2021) AE source localization and imaging on cylindrical shell structures based on six-AE-sensor monitoring network and VTR focusing imaging. Nondestruc Test Eval 36(1):35–61

Zheng YQ, Chen Y, Wang JH, Shang XY, Liu CY (2022) Acoustic emission localization method for complex structure based on improved interaction distance and Dijkstra algorithm and its application. Gold Sci Technol 30(3):427–437

Zhou J, Shen X, Qiu Y et al (2021) Improving the efficiency of microseismic source locating using a heuristic algorithm-based virtual field optimization method. Geomech Geophys Geo-Energ Geo-Resour 7(3):89